RSC Advances

PAPER

View Article Online
View Journal | View Issue

Open Access Article. Published on 05 January 2021. Downloaded on 1/13/2026 12:00:14 AM.
This article is licensed under a Creative Commons Attribution-NonCommercial 3.0 Unported Licence.

Check for updates

Cite this: *RSC Adv.*, 2021, **11**, 1586

Synthesis, characterisation and functionalisation of BAB-type dual-responsive nanocarriers for targeted drug delivery: evolution of nanoparticles based on 2-vinylpyridine and diethyl vinylphosphonate†

Andreas Saurwein,‡ Andreas Schaffer,‡ Christina Wieser and Bernhard Rieger *

The emerging field of nanomedicine gives new opportunities in the treatment of cancer. Aspects such as dosage, bioavailability or the application to the patient can be drastically improved. Previously our group reported an efficient route towards cross-linked nanospheres based on ABB′ block copolymers made from 2-vinylpyridine (2VP), diethyl vinylphosphonate (DEVP) and diallyl vinylphosphonate (DAlVP). Followed by thiol–ene click chemistry stable nanoparticles were formed. Herein, this promising concept was extended to copolymers with the analogous B′BABB′ architecture. In this context the new yttrium complex **5** was investigated in the rare-earth metal-mediated group transfer polymerisation (REM-GTP) and used for the generation of copolymers with different monomer feeds (2VP: 100–300 equiv.; DEVP: 200–300 equiv.; DAlVP: 6–20 equiv.) to explore the influence of the copolymer compositon on the nanoparticle properties. After successful cross-linking with various cross-linking agents, all nanoparticles were characterised *via* DLS and TEM. These size measurements revealed defined, almost spherical particles (d_{DLS} = 17–52 nm; d_{TEM} = 17–43 nm) and were mainly affected by the 2VP content and the cross-linking density. Zeta potential measurements resulted in values in the range from −6 mV to −22 mV and revealed an influence of the cross-linking agent on the surface charge. Studies on the release behaviour exhibited the fastest release at pH = 4.5. Temperature-wise best results were achieved at 42 °C. Furthermore, we aimed for the conjugation of folic acid as a model compound for a potential application in active drug targeting. The consecutive couplings of cysteamine and dithiol **6** enabled the formation of an amine-modified precursor which was reacted with a folic acid derivative. Zeta potential measurements and analysis by NMR spectroscopy corroborated a successful conjugation while DLS and TEM (d_{DLS} = 44 nm; d_{TEM} = 38 nm) indicated defined nanoparticles.

Received 19th October 2020
Accepted 5th December 2020

DOI: 10.1039/d0ra08902h

rsc.li/rsc-advances

Introduction

In the present-day cancer can be considered one of the biggest challenges to our modern society. Around 18 million new cancer cases and 9.6 million cancer-related deaths have been estimated for 2018 alone.[1] Common therapies can be divided into surgical removal, internal and external radiation and chemotherapy.[2] However, radiation and chemotherapy can be accompanied by severe side effects damaging normal tissue and organs as well as causing systemic toxicity owing to their inability to distinguish between healthy and cancer cells. Furthermore, the efficacy of the therapy can be highly individual despite a strictly identical treatment.[2–4]

Consequently, the treatment remains a complex task and demands improved, patient-friendly approaches since, for example, a study of Schiller *et al.* in 2002 implied that a therapeutic plateau was reached regarding the use of chemotherapeutics.[5,6] One promising development that aims to overcome this set of problems are nanosized drug-delivery vehicles. Currently, anticancer drugs are frequently limited owing to their high hydrophobicity and thus low solubility in aqueous media. Therefore, high tissue concentrations are required and can lead to systemic toxicity. Moreover, low molecular-weight agents are often eliminated by the liver or kidneys.[2,7] Drug-delivery vehicles allow the encapsulation of such hydrophobic substances, increase their bioavailability substantially and benefit from the enhanced permeability and retention (EPR)

WACKER-Chair of Macromolecular Chemistry, Catalysis Research Center, Technical University of Munich, Lichtenbergstraße 4, 85748 Garching Near Munich, Germany. E-mail: rieger@tum.de

† Electronic supplementary information (ESI) available: Synthetic procedures, NMR spectra, ESI analysis of the oligomers, GPC traces, release data for copolymers **BAB1–3**, DLS and TEM analysis of **NP1**, **NP3–7**, and **NP-FA**. See DOI: 10.1039/d0ra08902h

‡ These authors contributed equally.

© 2021 The Author(s). Published by the Royal Society of Chemistry

Open Access Article. Published on 05 January 2021. Downloaded on 1/13/2026 12:00:14 AM.
This article is licensed under a Creative Commons Attribution-NonCommercial 3.0 Unported Licence.

effect which results in an improved accumulation at the tumour site. In addition, engineered nanoparticles are able to facilitate a controlled release of the drug.[2,8–13] One widely investigated approach focuses on polymeric micelles. These are usually composed of a hydrophilic shell such as poly(ethylene glycol) (PEG) or poly(*N*-vinyl pyrrolidone) (PVP) and a hydrophobic core (*e.g.* poly(propylene oxide) (PPO), poly(D,L-lactic acid) (PDLLA), poly(ε-caprolactone) (PεCL), poly(L-aspartate)) (PASA), which enable a loading of the pharmacologically active agent.[7,14] Exemplarily, the application of such a micellar carrier improved the concentration of paclitaxel significantly.[15]

From this broad basis, delivery vehicles made from smart materials emerge as next generation nanocarriers. Since cancerous tissue exhibits a slightly acidic environment (pH = 6.5–6.8) compared to healthy tissue (pH = 7.4) as well as elevated temperatures (hyperthermia), stimuli-responsive drug delivery vehicles can take advantage from the pathological conditions of the diseased tissue and use these triggers to enhance the drug release.[2,7] In this context formulations with poly(2-vinylpyridine) (P2VP) demonstrated a pH-stimulated degradation of the micellar system while P2VP-comprising polymerosomes showed the release of the encapsulated cargo upon protonation of the pyridine motifs.[16,17] Among the temperature-sensitive materials poly(*N*-isopropylacrylamide) (PNIPAAm) is commonly used and finds broad application in many biomedical fields. Consequently, PNIPAAm-based carriers were also investigated for their use as the hyperthermia-directed drug delivery vehicles.[18,19] However, PNIPAAm features a lower critical solution temperature (LCST) of 32 °C demanding copolymerisation to reach physiological range and it can show functional loss in biological fluids.[20,21] A rather new material class are polyvinylphosphonates, which are soluble in aqueous media, feature a tuneable LCST and exhibit high biocompatibility.[22,23] Our group was able to establish an efficient and precise route towards well-defined, high molecular-weight polyvinylphosphonates *via* rare earth metal-mediated group transfer polymerisation.[24–27] In 2016 this work concluded in the synthesis of BAB block copolymers consisting of P2VP and poly(diethyl vinylphosphonate) (PDEVP). These copolymers formed monodisperse and spherical micelles in aqueous solution and showed a pH as well as a temperature-triggered release of doxorubicin (DOX). Moreover *in vitro* studies revealed the internalisation of the DOX-loaded carriers into HeLa cells.[28] However, the self-assembly of micelles remains a concentration-dependent process and is always affected by the equilibrium with free, non-associated polymer chains. As a result, micelles are subjected to high dilution in the human body upon injection which shifts the equilibrium-state towards the free polymer resulting in the dissociation of the micellar structures.[29,30] This effect intensifies when the unimers bind to other constituents, *e.g.* proteins or membranes.[30]

To avoid this issue, the basic concept of these nanocarriers was optimised by the introduction of diallyl vinylphosphonate (DAlVP) as a third block resulting in copolymers with an ABB′ block structure. The allyl groups facilitated the cross-linking of the copolymers *via* thiol–ene click chemistry and yielded stable, monodisperse and spherical particles. Most importantly the stimuli-triggered release was retained after cross-linking. In addition *in vitro* experiments gave evidence for the internalisation of the carriers into the cells and a statistic insight on the uptake level.[31] In this context we adopted the cross-linking procedure for BAB-type block copolymers and investigated the effects of the changed polymer architecture on the particle formation and the release behaviour. Moreover, folic acid was conjugated to the particles as a targeting ligand.

Results and discussion

Complex synthesis

In order to change the copolymer architecture from the ABB′ structure (A: 2VP, B: DEVP, B′: DAlVP) to a B′BABB′ block structure, a binuclear catalyst is required. Such a structure can be achieved *via* performing C–H bond activations with bifunctional initiators such as 2,3,5,6-tetramethylpyrazine (TMPy) (**1**).[32] Besides TMPy, 2,3-dimethylpyrazine (**2**) and 2,5-dimethylpyrazine (**3**) were also considered as possible initiators (Scheme 1a). The two opposing methyl groups of **1** located next to the heteroaromatic nitrogen presumably allow the C–H bond activation with $Cp_2Y(CH_2TMS)(THF)$ (**4**) and resulted in a complex comprising two catalytically active sites. Surprisingly, the use of pyrazines **2** and **3** did not result in a successful activation and led only to the formation of degradation products. Fortunately, mixing of the Cp_2Y complex **4** with TMPy immediately resulted in an intense orange colouration of the solution that indicated the σ-bond metathesis (Scheme 1b). The respective ^{1}H-NMR spectrum of the isolated complex strongly suggests the presence of only one species (Fig. 1). Most importantly, the signals at 1.99 and 2.91 ppm can be attributed to the CH_2Y and CH_3 groups and exhibit a 4 : 6 ratio. Additionally, one THF molecule must be coordinated to each yttrium centre. These observations are supported by ^{13}C-NMR spectroscopy as well as elemental analysis (EA). Moreover, NOESY NMR supports the formation of a single species with both methyl groups being spatially adjacent to each other (Fig. S3†). The kinetic analysis of the C–H bond activation *via* NMR revealed the full conversion after 18 hours (Fig. S4†).

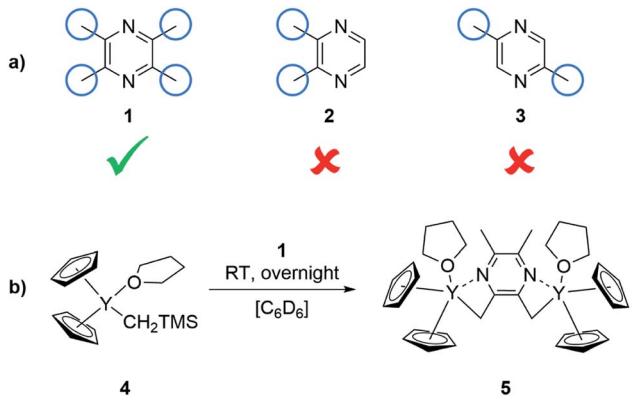

Scheme 1 (a) Screening of bifunctional pyrazines for the synthesis of a binuclear complex for REM-GTP. (b) Synthesis of the complex **5** with TMPy starting from $Cp_2Y(CH_2TMS)(THF)$ (**4**).

Open Access Article. Published on 05 January 2021. Downloaded on 1/13/2026 12:00:14 AM.
This article is licensed under a Creative Commons Attribution-NonCommercial 3.0 Unported Licence.

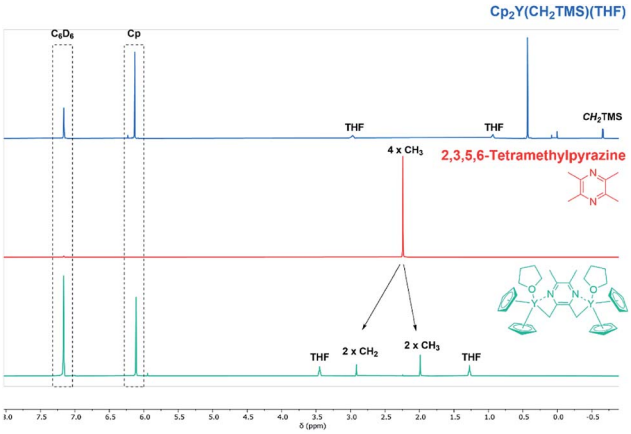

Fig. 1 Overview of C–H bond activation showing complex **4** (blue), TMPy (**1**) (red) and species **5** gained after completed C–H bond activation (green). ^{1}H-NMR spectra were recorded in benzene-d_6.

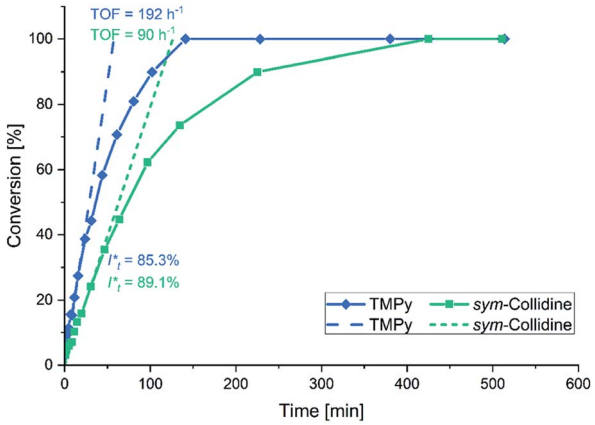

Fig. 2 Conversion-time plot for the polymerisation of 2VP with the TMPy activated complex **5** (blue) and with *sym*-collidine activated Cp_2Y (green).

End-group analysis

Since the lanthanide-based complexes activated with *sym*-collidine showed the incorporation of the initiator in the polymer chain, evidence was needed to prove the covalent integration of TMPy into the polymer chain.[25] By default, the characterisation of the end-group can be performed by electron spray ionisation mass spectrometry (ESI-MS) *via* analysis of the respective oligomer patterns. Three oligomer patterns were identified in the corresponding ESI-MS spectrum of the oligomers which were produced with complex **5** (Fig. S5†). The *m*/*z* values assigned to the first pattern show oligomer peaks ionised with H^+ (452 and 557 u) with a difference equal to the molecular mass of 2VP ($m_{2VP} = 105$ u). The second pattern with $z = 2$ was ionised by two protons and shows the respective oligomer signals (331, 384, 436, 489, and 541 u) with a difference of 52.5 u which is equivalent to the half of m_{2VP}. In addition, a third series of oligomer signals (291, 326, 361, and 396 u) can be attributed to $z = 3$. Thus, the mass difference was determined to be 35 u. For completeness, the ESI-MS spectrum generated with $Cp_2Y(CH_2(C_5H_2Me_2N))$ is illustrated in Fig. S6 in the ESI.†

Kinetic investigation of the TMPy-activated catalyst

In this context *sym*-collidine or TMPy were already employed as initiators in the polymerisation of 2VP with bisphenolate-based yttrium complexes by our group and alkyl yttrium complexes from Mashima *et al.*[33,34] As the C–H bond activated Cp_2Y complexes have not been evaluated in kinetic experiments with this monomer, the polymerisation of 2VP was investigated with the new complex **5**. Fig. 2 shows the conversion-time plot of complex **5** in blue. Hereby a turnover frequency (TOF) of 192 h^{-1} was determined while the corresponding initiator efficiencies (IE) were found to be 85% at the beginning and 88% at the end of the polymerisation. The living fashion of the polymerisation was able to be observed which is represented by the linear growth of the molecular weight. The corresponding polydispersites $Đ$ remained low with values $Đ < 1.10$ (Fig. 3). For a better classification, the kinetic measurements were also performed with the *sym*-collidine activated yttrium complex. The respective conversion-time plot is illustrated by the green curve in Fig. 2. In this case a TOF of 90 h^{-1} was determined. Concerning the initiator efficiency, a value of 89% was calculated at the start of the polymerisation and 72% at the end. As expected, the growth was found to be linear and showed low polydispersities between $Đ = 1.01$ and 1.12 (Fig. S7†). The kinetic data on the turnover frequencies appear to be in good agreement with the molecular structures of **5** and the complex with *sym*-collidine. Since **5** has two active sites attached to one initiator group after C–H bond activation the polymer chain can grow in two directions while *sym*-collidine can only bear one yttrium centre. This results in a TOF twice as high for complex **5**. Compared to the literature, the catalysts activated with TMPy or *sym*-collidine exhibit TOF values which are about three or 10 times lower than the bisphenolate system.[28,35] This finding might be explained by an improvement of the electronic properties of the metal centre induced by the bisphenolate ligand.

Copolymerisation results

Based on the complex analysis and kinetic findings a variety of copolymers were synthesised that were later conducted to the

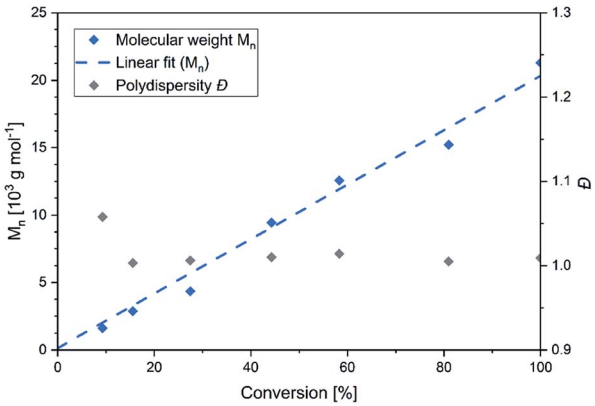

Fig. 3 Conversion-dependant plot of the molecular weights and corresponding polydispersities $Đ$ of P2VP generated with complex **5**.

 © 2021 The Author(s). Published by the Royal Society of Chemistry

Open Access Article. Published on 05 January 2021. Downloaded on 1/13/2026 12:00:14 AM.
This article is licensed under a Creative Commons Attribution-NonCommercial 3.0 Unported Licence.

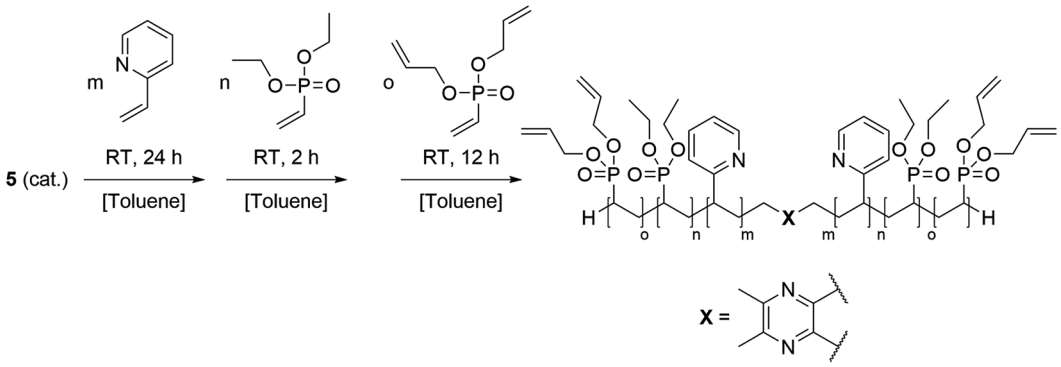

Scheme 2 Synthesis of the BAB block copolymers from 2VP, DEVP, and DAlVP *via* REM-GTP with catalyst **5**.

Table 1 Feed composition, monomer conversions, molecular weights M_n of block (A) and polydispersities $Đ$ for (A) and (BAB), initiator efficiencies IE of block (A) and composition of the copolymer

	Feed A/B/B′[a]/ equiv.	X (A)[b]/%	M_n (A)[c]/ 10^4 g mol^{-1}	$Đ$ (A)[c]/-	IE (A)[d]/%	X (B)[b]/%	Composition A/B [2VP/DEVP][b]	$Đ$ (BAB)[c]/—	M_n (B′BABB′)[b]/ 10^4 g mol^{-1}
BAB1	100/200/10	>99	1.21	1.05	94	>99	1.0/1.9	1.08	4.80
BAB2	200/200/10	>99	2.24	1.08	95	>99	1.0/1.1	1.10	5.90
BAB3	300/300/10	>99	2.97	1.04	>99	>99	1.0/1.1	1.07	8.12
BAB4	200/200/6	>99	2.76	1.06	80	>99	1.0/1.0	1.01	6.91
BAB5	200/200/20	>99	2.10	1.03	>99	>99	1.0/1.0	1.01	5.65

[a] By weighing the monomer, [M]/[cat.] = equiv. A: 2VP, B: DEVP, B′: DAlVP. [b] Conversions X were calculated from the corresponding ^{1}H-NMR or ^{31}P-NMR spectra. [c] Determined *via* GPC analysis in DMF. [d] Initiator efficiency IE was determined for block (A), IE = $M_{n,theo}/M_{n,exp}$.

cross-linking procedure (Scheme 2). In this work the monomer feed of 2VP and DEVP was varied between 100 equiv. and 300 equiv., while a feed ratio of 1 : 1 or 1 : 2 was adjusted. Furthermore, the DAlVP content was adjusted between six and 20 equiv. (Table 1). Each step of the copolymerisation was allowed to reach full conversion, which took approximately 24 hours in case of 2VP and two hours and 12 hours for DEVP and DAlVP, respectively (Scheme 2). Owing to the controlled nature of REM-GTP, all polymers showed narrow polydispersities ranging from $Đ$ = 1.01 to 1.10 and had molecular weights between 48.0 and 81.2 kg mol^{-1}, which exceeds the threshold for renal clearance of 40 kg mol^{-1}. The initiator efficiencies were calculated after determination of the P2VP block length and ranged around 90%. In addition, ^{1}H-NMR spectroscopy allowed the calculation of the experimental block ratios that match the theoretical block ratios very well. Here too, the signals of the allylic side groups were attributed *via* ^{1}H-NMR spectra between 4.50 and 6.00 ppm and are in good agreement with the previously published ABB′ based copolymers (Fig. 4, blue spectrum).

Nanoparticle formation *via* thiol–ene click chemistry

Cross-linking of the copolymers was performed *via* an established route using thiol–ene click chemistry with azobisisobutyronitrile (AIBN) as an initiator and 3,6-dioxa-1,8-octanedithiol (**6**),[31] 1,4-butanedithiol (**7**), or D,L-dithiothreitol (**8**) as a linking component (Scheme 3). As visualised in Fig. 4 the reaction was monitored *via* ^{1}H-NMR and was considered to reach full conversion after complete disappearance of the allylic protons. Since the cross-linking of the ABB′ copolymers was performed with an excess of dithiol **6**, we aimed for an optimisation by testing several dithiol amounts (3.0 equiv., 1.5 equiv., 1.0 equiv.) corresponding to the allyl group content of copolymer **BAB2**. As expected, an excess of three equivalents reached full conversion after 24 hours. But already a slight excess of the dithiol (1.5 equiv.) suffices to detect a complete reaction after the 24 hours. However, an amount of one equivalent appeared to be

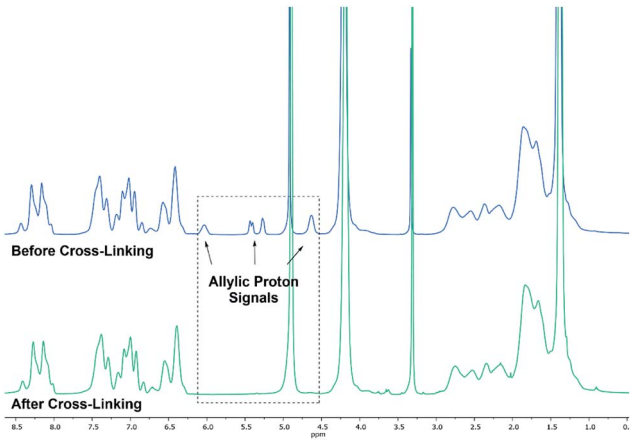

Fig. 4 Comparison of ^{1}H-NMR spectra before (**BAB2**) (blue) and after cross-linking (**NP2**) with 3,6-dioxa-1,8-octanedithiol (**6**) (green). Spectra were recorded in MeOD-d_4.

Open Access Article. Published on 05 January 2021. Downloaded on 1/13/2026 12:00:14 AM.
This article is licensed under a Creative Commons Attribution-NonCommercial 3.0 Unported Licence.

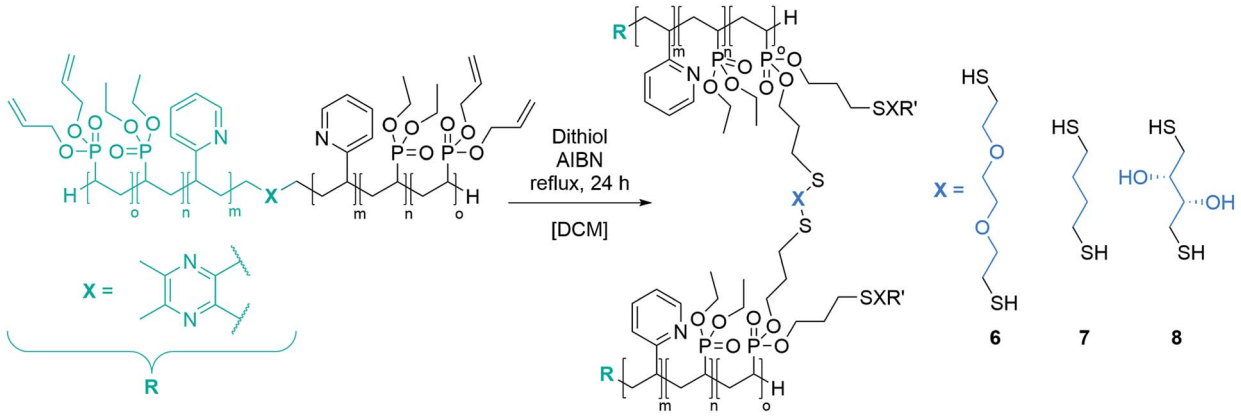

Scheme 3 Strategy for the cross-linking of the copolymers *via* thiol–ene click chemistry with dithiol **6**, **7** and **8**.

Table 2 Used copolymers and dithiols, diameters and polydispersities determined *via* DLS and TEM and zeta potential ζ of the nanoparticles

	Polymer	Dithiol	*d* (DLS)/nm	PDI (DLS)	ζ/mV	*d* (TEM)/nm	PDI (TEM)
NP1	**BAB1**	**6**	21.1 ± 0.9	0.17	−11 ± 0.3	17.1 ± 1.6	0.09
NP2	**BAB2**	**6**	32.6 ± 0.4	0.19	−13 ± 0.2	31.0 ± 4.7	0.15
NP3	**BAB3**	**6**	51.9 ± 3.9	0.16	−19 ± 1.0	42.7 ± 4.9	0.11
NP4	**BAB4**	**6**	41.7 ± 5.6	0.17	−16 ± 0.6	34.2 ± 2.3	0.08
NP5	**BAB5**	**6**	16.8 ± 0.6	0.22	−22 ± 0.5	26.1 ± 2.4	0.09
NP6	**BAB3**	**7**	47.4 ± 3.8	0.16	−9.8 ± 0.4	41.1 ± 5.6	0.14
NP7	**BAB3**	**8**	46.9 ± 1.8	0.13	−6.3 ± 0.2	41.0 ± 3.9	0.09

insufficient because traces of the allylic protons were still visible. After optimisation of the dithiol amount the successfully cross-linked samples were analysed *via* transmission electron microscopy (TEM) and dynamic light scattering (DLS) to verify the formation of the nanoparticles. Table 2 gives an overview of the experimental data of the generated nanoparticles. With the exception of **NP1** and **NP5**, all cross-linked particles exhibit diameters larger than 30 nm with particle sizes between 32.6 and 51.9 nm. These values match with data of earlier reports that recommend a size range of 30–100 nm for an optimised targeting of the cancerous tissue because nanocarriers of this size benefit from the EPR effect and they are too large for renal clearance.[36,37] Concerning the size distribution, PDIs ≤ 0.22 were found which slightly deviates from an optimal PDI below 0.10. Nevertheless, imaging *via* TEM indicates highly uniform and monodisperse, spherical particles. Furthermore, the size-related values gained with both methodologies are in good accordance with each other (Table 2). The DLS and TEM data of **NP2** are illustrated in Fig. 5. The remaining data are summarized in the ESI (Fig. S26, S29, S31, S33, S35, S38).† As shown by **NP1–3**, the particle size is mainly influenced by the P2VP block while a change of the DEVP block only has minor influence on the diameter. Moreover, a decrease of the DAlVP amount resulted in a larger diameter for **NP4** compared to **NP2**, while **NP5** exhibited a much smaller diameter. Therefore, it can be concluded that the spatial extent of the particles can be tuned by the cross-linking density. The type of cross-linker has no significant influence on the particle size. Additional zeta

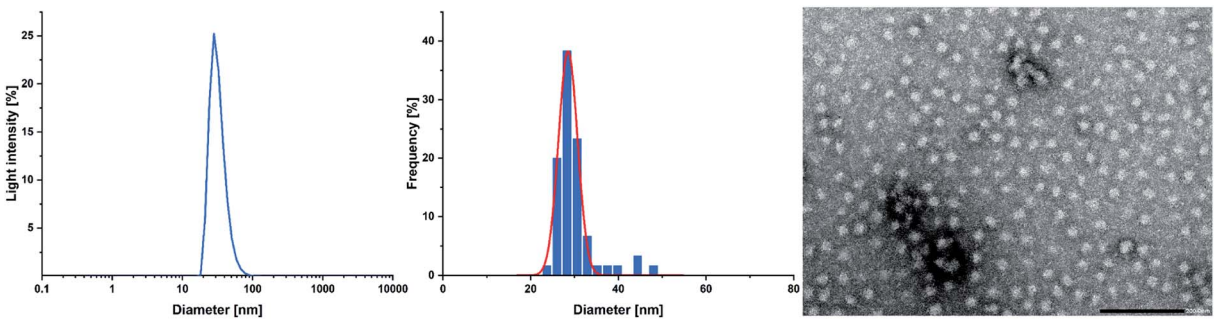

Fig. 5 Size distribution of **NP2** determined *via* DLS measurements at a concentration of 2.5 mg mL^{-1} in water (left); histogram plot with a Gaussian regression fit (middle); and a TEM image of **NP2** (right) with a scale bar of 200 nm.

 © 2021 The Author(s). Published by the Royal Society of Chemistry

Open Access Article. Published on 05 January 2021. Downloaded on 1/13/2026 12:00:14 AM.
This article is licensed under a Creative Commons Attribution-NonCommercial 3.0 Unported Licence.

potential measurements attribute a negative surface charge for the particles between −22 and −6.3 mV. A negative charge was also observed for the ABB′-type nanoparticles.[31] However, **NP6** and **NP7** tend to have potentials closer to zero than the ones with **6** as cross-linker. Generally speaking, a positive surface charge is preferable because of the anionic character of the cellular membrane. However, this is contradicted by an increasing cytotoxicity and a higher affinity towards vascular endothelial cells and other anionic species which leads to aggregation and a corruption of the potential therapeutic effects.[38–40] However, in 2008 Huang *et al.* demonstrated a slower clearance of neutral carriers compared to their anionic pendants, which indicated a surface charge near zero would be beneficial for drug delivery.[31,41] Additionally, measurements in $CHCl_3$ were performed to test the stability of the particles because both blocks are soluble in $CHCl_3$ (Fig. S41†). In case of **NP1–NP6** the particle diameters exceeded those values that were determined in water. Therefore, stable particles can be assumed since the free polymer chains should form random coils in solution which must be much smaller than the respective nanoparticles. However, the cross-linking of **BAB3** to **NP7** appeared not to be successful because a diameter of only 12.6 nm was determined compared to 46.9 nm in water.

Release behaviour of the nanoparticles

Eventually the loading and release behaviour of the nanoparticles was studied. After loading with fluorescein, the samples were analysed in respect of the cumulative release by dialysis. For this purpose, varying temperatures and pH-values were adjusted. For that purpose, room temperature and a neutral pH were adjusted as reference. A temperature of 37 °C was set to simulate the body temperature, while 42 °C was used to mimic hyperthermic conditions caused by cancer cells. With regard to the pH, acidic environments were adjusted to simulate the conditions in the endosomal environment (pH = 6.0) or the interior of the lysosome (pH = 4.5).[31,42] In Fig. 6 the cumulative fluorescein release of **BAB2** and **NP2** is visualised. Compared to the micelles formed from **BAB2** the release from the cross-linked nanoparticle **NP2** was improved by approximately 20% after 30 hours. In both cases elevated temperatures as well as acidic conditions stimulated the release compared to the standard scenario at room temperature and a neutral environment. Regarding the temperature, a coil-to-globule-transition triggers the collapse of the DEVP-based shell. Unfortunately, there is no

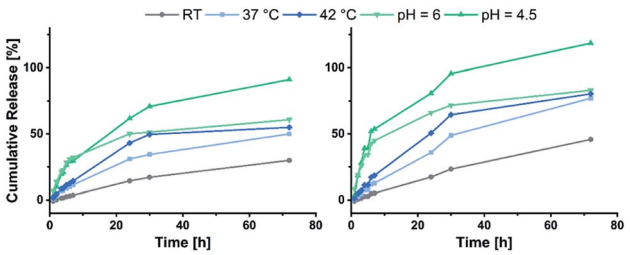

Fig. 6 Cumulative release of fluorescein from BAB2 (left) in comparison to NP2 (right).

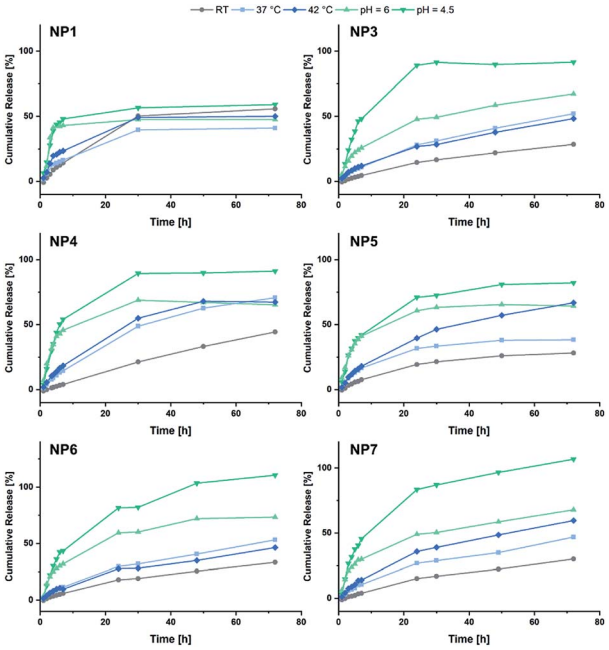

Fig. 7 Summary of the cumulative fluorescein release from NP1 and NP3–NP7.

significant differentiation between 37 °C and 42 °C. Overall best results were obtained at pH = 4.5. But whereas **BAB2** revealed a quantitative release after 70 hours, this was already achieved after 30 hours with **NP2**. The release data of nanoparticles **NP1** and **NP3–NP7** are illustrated in Fig. 7. Interestingly, **NP1** shows inferior characteristics with a cumulative release limited to approximately 50% in all scenarios after 30 hours. This might be attributed to a relatively rigid and inflexible structure of **BAB1** with its short P2VP core, which prevents the release of the cargo. **NP3** exhibited best results at acidic conditions and showed a quantitative release of fluorescein after 24 hours at pH = 4.5 and 60% after 70 hours at pH = 6.0. Hence, **NP3** must be most sensitive to conformational changes upon protonation of the pyridine units which promotes the release of the cargo as it has the largest P2VP block. **NP4** and **NP5** also showed best results at a pH of 4.5 with a cumulative release between 80 and 90%, but both nanoparticles also seem to be quite responsive to changes in temperature and outperform **NP3** in this category. **NP4** reaches a release of approximately 70% but shows no differentiation between 37 and 42 °C on the one hand. On the other hand, **NP5** features a distinctive gap of the releases at 37 °C (30%) and 42 °C (70%). Therefore, a tightly cross-linked particle shell might be beneficial in terms of a temperature-triggered release. The release behaviour of **NP6** and **NP7** corresponds with the results of **NP3** regarding the rate and extent of the release. However, the non-polar cross-linker 1,4-butanedithiol (7) seems to decrease the temperature-induced release of fluorescein.

Shell-functionalisation with folic acid

To broaden the scope of this concept the nanocarriers should be developed towards an application in active targeting. Such

Open Access Article. Published on 05 January 2021. Downloaded on 1/13/2026 12:00:14 AM.
This article is licensed under a Creative Commons Attribution-NonCommercial 3.0 Unported Licence.

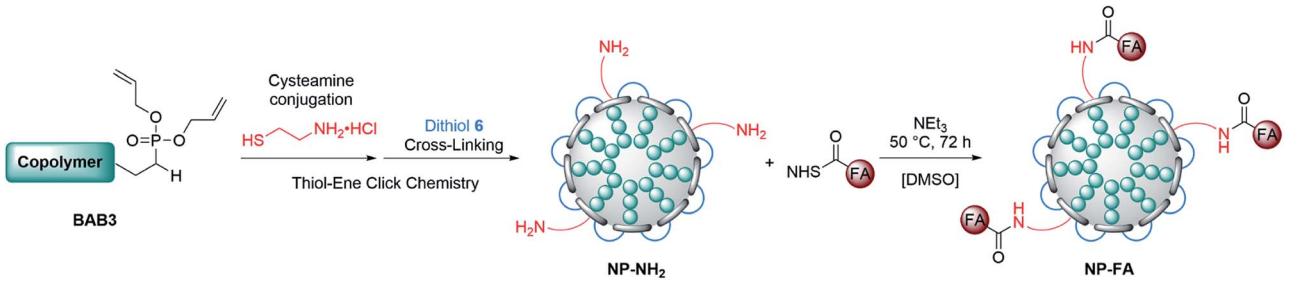

Scheme 4 Strategy for the introduction of shell-bound folic acid *via* partial conversion of the allyl groups with cysteamine hydrochloride. Folic acid was conjugated using an NHS-ester of folic acid after the cross-linking with dithiol **6**.

a type of nanoparticle requires the presence of superficial targeting ligands which can be recognised and bind to disease-specific cell features.[8] Folic acid is a prominent example for such a targeting ligand and shows high affinity to its folate-receptor ($K_d < 10^{-9}$) which is overexpressed on many cancer types,[43] and is therefore a beneficial targeting motif for the development of novel therapeutic concepts.[44–47] The conjugation of folic acid was achieved by the formation of a NH_2-bearing nanoparticle **NP-NH$_2$**. As depicted in Scheme 4 the allyl functions of **BAB3** were functionalised with cysteamine-hydrochloride first and cross-linked with dithiol **6** *via* thiol–ene chemistry to yield an amino-group containing surface. This reaction sequence was monitored *via* ^{1}H-NMR (Fig. S43†) and revealed a partial consumption of the allyl groups in the first step. Treatment of this precursor with the dithiol resulted in the quantitative conversion of the remaining allyl signals. With a zeta potential of −18 mV, **NP-NH$_2$** stayed in the same region as **NP3** (−19 mV). Subsequently, the particles were converted with the *N*-hydroxysuccinimide (NHS) ester of folic acid to form **NP-FA**. The NHS ester was employed in large excess to ensure a reaction with the surface-bound amino groups. After purification by dialysis, the ^{1}H-NMR exhibited characteristic signals of folic acid at 4.49 (CH_2NH), 6.64, 7.65 (both *p*-aminobenzoic acid) and 8.65 ppm (pteridine) (Fig. 8 and S45†). The zeta potential increased to −11 mV, which indicates a modification

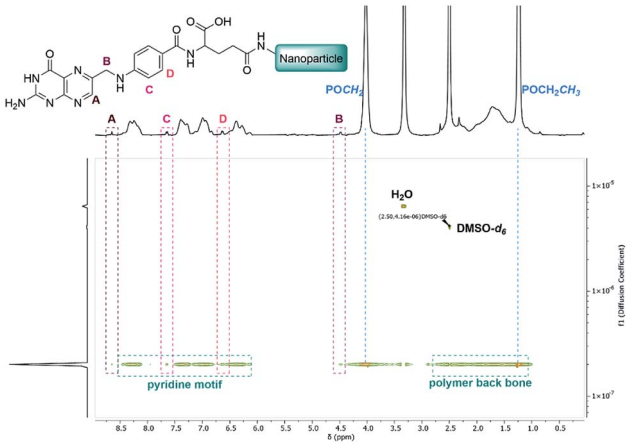

Fig. 8 DOSY-NMR spectrum of the folate-modified nanoparticle **NP-FA** in DMSO-d_6.

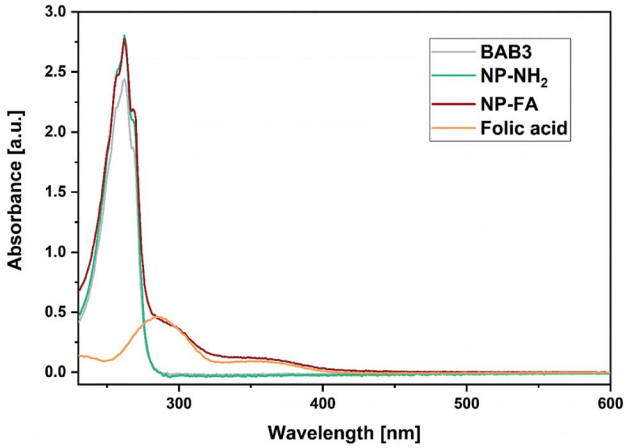

Fig. 9 UV/Vis spectra of **BAB3** (1.25 mg mL^{-1}), **NP-NH$_2$** (1.25 mg mL^{-1}), **NP-FA** (1.25 mg mL^{-1}), and free folic acid (100 μM) in methanol.

of the surface features of the particle shell. Diffusion-ordered spectroscopy (DOSY) was also performed to verify further the conjugation of folic acid. In the corresponding spectrum the folic acid related signals share the same diffusion coefficient ($D = 2.00 \times 10^{-7}$ m^2 s^{-1}) with the polymer-related signals from the polymer blocks. Additional characterisation by DLS and TEM confirmed the formation of spherical, almost uniform particles (Fig. S44†). The diameters were found to be 44.4 ± 0.9 (PDI = 0.11) for DLS and 38.2 ± 3.1 (PDI = 0.08) for TEM, respectively. In comparison to the non-modified analogues **NP3**, **NP6** or **NP7**, the diameters of **NP-FA** are slightly lower. Lastly, analysis by UV/Vis revealed the absorption band of folic acid at 360 nm, which was not visible for the copolymer **BAB3** and the precursor particle **NP-NH$_2$** (Fig. 9).

Conclusions

In summary, we expanded the scope of the ABB′-type (A: 2VP; B: DEVP, B′: DAlVP) nanoparticles towards a B′BABB′ architecture by using TMPy (**1**) as an initiator. The resulting complex **5** exhibited a TOF of 192 h^{-1} with 2VP and generated copolymers **BAB1–BAB5** with high precision by a GTP-type propagation mechanism. The copolymers were then cross-linked to **NP1–NP7** with three dithiols *via* thiol–ene click chemistry and formed defined particles in aqueous solution (d = 16.8–

 © 2021 The Author(s). Published by the Royal Society of Chemistry

Open Access Article. Published on 05 January 2021. Downloaded on 1/13/2026 12:00:14 AM.
This article is licensed under a Creative Commons Attribution-NonCommercial 3.0 Unported Licence.

51.9 nm, PDI = 0.13–0.22), which was confirmed by transmission electron microscopy. The particle diameters were mostly determined by the copolymer composition, while the choice of the cross-linker influenced the zeta potential of the shell. Elevated temperatures and acidic conditions improved the release of fluorescein as the corresponding release studies have revealed. Throughout all experiments, the strongest response was observed at a pH = 4.5. Temperature-wise **NP2**, **NP4** and **NP5** were most promising with respect to hyperthermia treatments. Moreover, we presented a facile synthesis approach towards nanoparticles with surface-bound folic acid, which was accomplished by the incorporation of cysteamine on the particle surface. As a result, the shell-located amino groups enabled the coupling of the activated folic acid derivative. The conjugation of such a ligand is a prerequisite for the application as targeted drug delivery vehicles. In addition, this synthetic strategy can be used to form tailor-made nanoparticles with selected targeting ligands that consider the molecular characteristics of the respective disease.

Conflicts of interest

There are no conflicts to declare.

Acknowledgements

The authors thank Laura Fuchs and Simone Poprawa for their support with the experiments and kinetic measurements, Dr Carsten Peters for his efforts to get the best TEM images, Dr Friederike Adams for the productive discussions and her helpful input and Alina Denk and Christopher Thomas for revising the manuscript.

Notes and references

1 F. Bray, J. Ferlay, I. Soerjomataram, R. L. Siegel, L. A. Torre and A. Jemal, *Ca-Cancer J. Clin.*, 2018, **68**, 394–424.
2 T. Sun, Y. S. Zhang, B. Pang, D. C. Hyun, M. Yang and Y. Xia, *Angew. Chem., Int. Ed.*, 2014, **53**, 12320–12364.
3 S. M. Bentzen, *Nat. Rev. Cancer*, 2006, **6**, 702.
4 D. Peer, J. M. Karp, S. Hong, O. C. Farokhzad, R. Margalit and R. Langer, *Nat. Nanotechnol.*, 2007, **2**, 751.
5 J. H. Schiller, D. Harrington, C. P. Belani, C. Langer, A. Sandler, J. Krook, J. Zhu and D. H. Johnson, *N. Engl. J. Med.*, 2002, **346**, 92–98.
6 J. Zugazagoitia, C. Guedes, S. Ponce, I. Ferrer, S. Molina-Pinelo and L. Paz-Ares, *Clin. Ther.*, 2016, **38**, 1551–1566.
7 C. Oerlemans, W. Bult, M. Bos, G. Storm, J. F. W. Nijsen and W. E. Hennink, *Pharm. Res.*, 2010, **27**, 2569–2589.
8 F. X. Gu, R. Karnik, A. Z. Wang, F. Alexis, E. Levy-Nissenbaum, S. Hong, R. S. Langer and O. C. Farokhzad, *Nano Today*, 2007, **2**, 14–21.
9 K. Cho, X. Wang, S. Nie, Z. Chen and D. M. Shin, *Clin. Cancer Res.*, 2008, **14**, 1310–1316.
10 S. Kalepu and V. Nekkanti, *Acta Pharm. Sin. B*, 2015, **5**, 442–453.
11 H. Maeda, J. Wu, T. Sawa, Y. Matsumura and K. Hori, *J. Controlled Release*, 2000, **65**, 271–284.
12 Y. Matsumura, *Adv. Drug Delivery Rev.*, 2008, **60**, 899–914.
13 O. C. Farokhzad and R. Langer, *ACS Nano*, 2009, **3**, 16–20.
14 D. Sutton, N. Nasongkla, E. Blanco and J. Gao, *Pharm. Res.*, 2007, **24**, 1029–1046.
15 K. M. Huh, S. C. Lee, Y. W. Cho, J. Lee, J. H. Jeong and K. Park, *J. Controlled Release*, 2005, **101**, 59–68.
16 A. Karanikolas, P. Tsolakis, G. Bokias and C. Tsitsilianis, *Eur. Phys. J. E*, 2008, **27**, 335–343.
17 U. Borchert, U. Lipprandt, M. Bilang, A. Kimpfler, A. Rank, R. Peschka-Süss, R. Schubert, P. Lindner and S. Förster, *Langmuir*, 2006, **22**, 5843–5847.
18 Y. Qu, J. Li, J. Ren, J. Leng, C. Lin and D. Shi, *Nanoscale*, 2014, **6**, 12408–12413.
19 H. Wei, S.-X. Cheng, X.-Z. Zhang and R.-X. Zhuo, *Prog. Polym. Sci.*, 2009, **34**, 893–910.
20 L. Zha, B. Banik and F. Alexis, *Soft Matter*, 2011, **7**, 5908–5916.
21 E. Roux, M. Francis, F. M. Winnik and J.-C. Leroux, *Int. J. Pharm.*, 2002, **242**, 25–36.
22 C. Schwarzenböck, A. Schaffer, P. Pahl, P. J. Nelson, R. Huss and B. Rieger, *Polym. Chem.*, 2018, **9**, 284–290.
23 N. Zhang, S. Salzinger and B. Rieger, *Macromolecules*, 2012, **45**, 9751–9758.
24 U. B. Seemann, J. E. Dengler and B. Rieger, *Angew. Chem.*, 2010, **122**, 3567–3569.
25 B. S. Soller, S. Salzinger, C. Jandl, A. Pöthig and B. Rieger, *Organometallics*, 2015, **34**, 2703–2706.
26 S. Salzinger, U. B. Seemann, A. Plikhta and B. Rieger, *Macromolecules*, 2011, **44**, 5920–5927.
27 S. Salzinger, B. S. Soller, A. Plikhta, U. B. Seemann, E. Herdtweck and B. Rieger, *J. Am. Chem. Soc.*, 2013, **135**, 13030–13040.
28 P. T. Altenbuchner, P. D. L. Werz, P. Schöppner, F. Adams, A. Kronast, C. Schwarzenböck, A. Pöthig, C. Jandl, M. Haslbeck and B. Rieger, *Chem.–Eur. J.*, 2016, **22**, 14576–14584.
29 A. Lavasanifar, J. Samuel and G. S. Kwon, *Adv. Drug Delivery Rev.*, 2002, **54**, 169–190.
30 C. F. van Nostrum, *Soft Matter*, 2011, **7**, 3246–3259.
31 C. Schwarzenböck, P. J. Nelson, R. Huss and B. Rieger, *Nanoscale*, 2018, **10**, 16062–16068.
32 F. Adams, P. T. Altenbuchner, P. D. L. Werz and B. Rieger, *RSC Adv.*, 2016, **6**, 78750–78754.
33 F. Adams, P. Pahl and B. Rieger, *Chem.–Eur. J.*, 2018, **24**, 509–518.
34 H. Kaneko, H. Nagae, H. Tsurugi and K. Mashima, *J. Am. Chem. Soc.*, 2011, **133**, 19626–19629.
35 F. Adams, M. R. Machat, P. T. Altenbuchner, J. Ehrmaier, A. Pöthig, T. N. V. Karsili and B. Rieger, *Inorg. Chem.*, 2017, **56**, 9754–9764.
36 Y. Matsumura and K. Kataoka, *Cancer Sci.*, 2009, **100**, 572–579.
37 J. Wang, W. Mao, L. L. Lock, J. Tang, M. Sui, W. Sun, H. Cui, D. Xu and Y. Shen, *ACS Nano*, 2015, **9**, 7195–7206.
38 R. Elul, *J. Physiol.*, 1967, **189**, 351–365.

Open Access Article. Published on 05 January 2021. Downloaded on 1/13/2026 12:00:14 AM.
This article is licensed under a Creative Commons Attribution-NonCommercial 3.0 Unported Licence.

39 A. Musyanovych, J. Dausend, M. Dass, P. Walther, V. Mailänder and K. Landfester, *Acta Biomater.*, 2011, **7**, 4160–4168.
40 E. Fröhlich, *Int. J. Nanomed.*, 2012, **7**, 5577–5591.
41 S.-D. Li and L. Huang, *Mol. Pharm.*, 2008, **5**, 496–504.
42 Y.-B. Hu, E. B. Dammer, R.-J. Ren and G. Wang, *Transl. Neurodegener.*, 2015, **4**, 18.
43 C. Chen, J. Ke, X. E. Zhou, W. Yi, J. S. Brunzelle, J. Li, E.-L. Yong, H. E. Xu and K. Melcher, *Nature*, 2013, **500**, 486–489.
44 C. M. Alexander, K. L. Hamner, M. M. Maye and J. C. Dabrowiak, *Bioconjugate Chem.*, 2014, **25**, 1261–1271.
45 B. Stella, S. Arpicco, M. T. Peracchia, D. Desmaële, J. Hoebeke, M. Renoir, J. D'Angelo, L. Cattel and P. Couvreur, *J. Pharm. Sci.*, 2000, **89**, 1452–1464.
46 X. Qiang, T. Wu, J. Fan, J. Wang, F. Song, S. Sun, J. Jiang and X. Peng, *J. Mater. Chem.*, 2012, **22**, 16078–16083.
47 S. Dong, H. J. Cho, Y. W. Lee and M. Roman, *Biomacromolecules*, 2014, **15**, 1560–1567.

 © 2021 The Author(s). Published by the Royal Society of Chemistry